DRAFT VERSION DECEMBER 12, 2023
Typeset using LaTeX **twocolumn** style in AASTeX63

Identification of Lensed Gravitational Waves with Deep Learning

KYUNGMIN KIM,[1] JOONGOO LEE,[1,2] ROBIN S. H. YUEN,[3] OTTO A. HANNUKSELA,[4,5] AND TJONNIE G. F. LI[3]

[1]*Korea Astronomy and Space Science Institute, 776 Daedeokdae-ro, Yuseong-gu, Daejeon 34055, Republic of Korea*
[2]*Department of Physics and Astronomy, Seoul National University, Seoul 08826, Republic of Korea*
[3]*Department of Physics, The Chinese University of Hong Kong, Shatin, New Territories, Hong Kong*
[4]*Nikhef - National Institute for Subatomic Physics, Science Park, 1098 XG Amsterdam, The Netherlands*
[5]*Department of Physics, Utrecht University, Princetonplein 1, 3584 CC Utrecht, The Netherlands*

ABSTRACT

The propagation path of gravitational waves (GWs) is expected to be bent near massive astrophysical objects. The massive object acts as a lens. Similarly to the lensing of electromagnetic waves, the lens amplifies GWs' amplitude and can produce multiple GW images. If we suppose the positions of lens and source of a GW deviate from the line of sight, the GW images arrive at different times because they have traveled different trajectories around the lens at the same speed. Depending on the difference in their arrival times, multiple GWs can be detected as repeated, near-identical events, or superposed GWs with characteristic "beating patterns". When the lens is small, $\lesssim 10^5 M_\odot$, it produces images with short time delays that result in the beating patterns. We utilize deep learning to study the lensing signature. It is known that state-of-the-art deep learning models are excellent at recognizing foreground images, similar to spectrograms of GWs, from background noises. We study the feasibility of applying deep learning to identify lensing signatures from the spectrogram of GW signals detectable by the Advanced LIGO and Virgo detectors. We assume the lens mass is around $10^3 M_\odot - 10^5 M_\odot$ which can produce the order of millisecond time delays between two images of lensed GWs. We discuss the feasibility of two aspects: distinguishing lensed GWs from unlensed ones and estimating the parameters related to the lensing. We suggest this work would be of particular interest for more complicated lensings for which we do not have accurate waveform templates.

Keywords: gravitational waves – gravitational lensing: weak – methods: data analysis – techniques: miscellaneous

1. INTRODUCTION

When gravitational waves (GWs) propagate near massive astrophysical objects such as black holes, substructures, galaxies or galaxy clusters, they become focussed or blurred by the result of gravitational lensing (Ohanian 1974; Bliokh & Minakov 1975; Bontz & Haugan 1981; Thorne 1983; Deguchi & Watson 1986; Nakamura 1998; Takahashi & Nakamura 2003). Gravitational lensing is verified by electromagnetic (EM) observations for decades and has led to groundbreaking findings in astrophysics. For example, it has resulted in the detection of exoplanets (Cassan et al. 2012) and has placed highly credible evidence for dark matter (Clowe et al. 2004; Markevitch et al. 2004). Meanwhile, in the field of GWs, lensing might present interesting applications in fundamental physics, astrophysics and cosmology as studied in the literature (Sereno et al. 2011; Jung & Shin 2019; Lai et al. 2018; Dai et al. 2018; Hannuksela et al. 2020).

The methods to detect lensed GWs have been developed in recent years and the first searches for GW lensing signatures in the LIGO and Virgo data were carried out (Hannuksela et al. 2019; Li et al. 2019; McIsaac et al. 2019; Pang et al. 2020; Dai et al. 2020). Lensing rate forecasts suggest that strongly lensed GWs could be detected by the Advanced LIGO (Aasi et al. 2015) and Virgo (Acernese et al. 2015) detectors upon reaching design sensitivity (Ng et al. 2018; Li et al. 2018; Oguri 2018). We expect even more detections in the Einstein Telescope (Punturo et al. 2010) or Cosmic Explorer (Reitze et al. 2019) where microlensing might also become more prominent (Diego et al. 2019). Therefore, it is timely to prepare all possible alternative methods for the identification of lensing signature imprinted in GW signals as many as possible. Note that there exists no complete waveform templates especially for the microlensed wave-

kkim@kasi.re.kr

forms that can currently be applied to LIGO/Virgo searches for lensing-induced beating patterns. For example, Lai et al. (2018) and Hannuksela et al. (2019) discussed the template-based search method under assuming isolated point mass lenses. However, it is conceivable that the beating patterns could be caused by more complicated lens setups, such as a field of microlenses within an external potential (see Diego et al. (2019) and Pagano et al. (2020)). Therefore, it is important to explore alternatives to the traditional templated searches.

To date, non-template-based search methods have been suggested in the literature. For example, Haris et al. (2018) has developed a method based on the Bayes factor to identify pairs of lensed GW signals under the strong lensing assumption (i.e. the mass of lens, $M_L \gtrsim 10^7 M_\odot$). This method has been applied for searching the lensing signature from the GW signals observed in the first and second observing runs of LIGO and Virgo (Hannuksela et al. 2019)). In the meantime, from a pedagogical study (Singh et al. 2019), the possiblity of applying machine learning to the discrimination of the lensed GW was discussed under the weak lensing assumption ($M_L \lesssim 10^7 M_\odot$). We have shown from the study that the superposed GW signals induced by the weak lensing can be distinguished from unlensed GWs with $> 90\%$ accuracy by virtue of supervised machine learning classifiers.

In this work, we improve the work of Singh et al. (2019) to make the approach to be practically applicable. To this end, we take into account more realistic considerations such as (i) using a realistic GW waveform generation method, (ii) considering the power spectral density (PSD) of the Advanced LIGO, (iii) constraining the optimal signal-to-noise ratio (SNR) to cover the SNRs of the 10 GWs from binary black hole mergers (BBH) which are reported in the GWTC-1 (Abbott et al. 2019), and (iv) using a conventional constant-Q transform method (Chatterji et al. 2004) in the generation of spectrogram samples. For the machine learning method, we use a state-of-the-art deep learning model, the Visual Geometry Group network (VGG) (Simonyan & Zisserman 2014), which is a variant of typical convolutional neural networks. The implementation of the VGG is done not only for the classification but also for the regression on the characteristic parameters of the lensed GWs. We show that $> 96\%$ of lensed GW samples are correctly classified and, from the regression, the averaged residual between the predicted parameters and the true parameters of the GW samples lensed by the singular isothermal sphere lens model is ~ 0.15.

This paper is organized as follows: we introduce a brief overview of considered lensing models in Sec. 2. We summarize the procedure from the preparation of input data to the application of VGG in Sec. 3. We present the results of the classification and regression in Sec. 4 and discuss this work and future direction in Sec. 5.

2. LENSED GRAVITATIONAL WAVES

Models for lensing of GWs have been studied for decades (Ohanian 1974; Bliokh & Minakov 1975; Bontz & Haugan 1981; Thorne 1983; Deguchi & Watson 1986; Schneider et al. 1992; Nakamura & Deguchi 1999; Takahashi & Nakamura 2003). Depending on the wavelength, λ, of the GW, the lensing effect can be categorized in two regimes: the geometrical optics limit is valid when λ is much shorter than the Schwarzschild radius of a lens. On the other hand, when λ is larger than the Schwarzschild radius of a lens, the diffraction effect becomes important and the wave optics limit holds for the regime (Takahashi & Nakamura 2003). The regime where each optics limit is valid also can be determined with respect to M_L. In Takahashi & Nakamura (2003), it is discussed that the diffraction effect becomes important when M_L satisfies

$$M_L \lesssim 10^8 M_\odot \left(f/\mathrm{mHz}\right)^{-1}. \tag{1}$$

If we regard the sensitive frequency band, 10^2 Hz – 10^3 Hz, of the Advanced LIGO and Virgo detectors, we can easily compute from Equation (1) that M_L in the range of $10^2 M_\odot$ – $10^3 M_\odot$ corresponds to the regime where the wave optics limit is valid. However, for the 10 GWs from the BBH in GWTC-1, no evidence of lensing signature originated by the wave optics effect was found for $M_L \lesssim 10^5 M_\odot$ (Hannuksela et al. 2019) and it is shown that the wave optics effect is typically negligible when M_L is $\sim 10^3 M_\odot - 10^4 M_\odot$ (Lai et al. 2018). Therefore, we suppose that there is still a possibility to see the geometrical optics effect in $10^3 M_\odot \lesssim M_L \lesssim 10^5 M_\odot$ and focus on the geometrical optics limit only in this work for simplicity.

The GW lensing theory is outlined in standard references such as Takahashi & Nakamura (2003). We start by assuming that the distances from an observer to a lens and to a source are far enough. Then, we can make use of the thin lens approximation where M_L is distributed over a two-dimensional plane perpendicular to the line of sight of the observer to the lens. In Figure 1, we illustrate a schematic configuration of the lensing of GW in the thin lens approximation. By the approximation, we can parameterize the displacement of source, γ, and the impact factor, ξ, with a single value, y, such as

$$y = \frac{\gamma D_L}{\xi_0 D_S}, \tag{2}$$

where $\xi_0 = \sqrt{(4GM_L/c^2) D_{LS} D_L / D_S}$ is the Einstein radius of a lens and D_L, D_S, and D_{LS} are the distances to the lens, to the source, and from the lens to the source, respectively.

With the above setup, the relation between the lensed GW, $h_L(f)$, and the unlensed GW, $h(f)$ in frequency domain can be written as

$$h_L(f) = F(f) h(f), \tag{3}$$

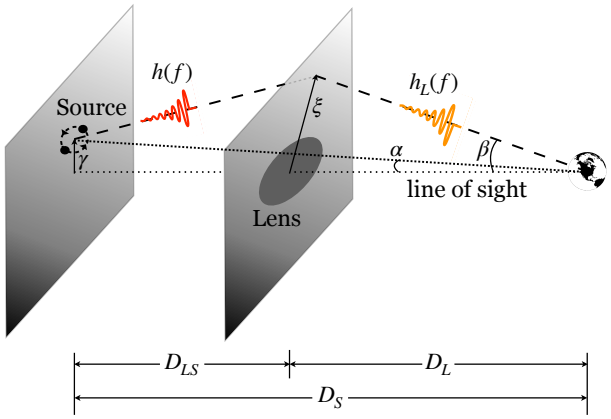

Figure 1. Schematic configuration of lensing of GW in the thin lens approximation where the angle, α and β are negligible. γ is the position of the source in the source plane which measures the displacement of the position of the source from the line of sight, ξ is the impact factor which can be normalized by the Einstein radius, ξ_0. D_L, D_S, and D_{LS} indicate the distances from observer to the lens, to the source, and from the lens to the source, respectively. The differences in colors on $h(f)$ and $h_L(f)$ represent the frequency dependent amplification effect in GW described in Equation (3).

where $F(f)$ is the amplification factor which can be determined by y and the surface mass density of lens.

For the surface mass density of a lens, we consider two simple lens models, the point mass lens model (PM) and the singular isothermal sphere lens model (SIS). In the geometrical optics limit, $F(f)$ of each model is written as

$$\text{PM}: F(f) = \sqrt{|\mu_+|} - i\sqrt{|\mu_-|}e^{2\pi i f \Delta t_d} \tag{4}$$

$$\text{SIS}: F(f) = \begin{cases} \sqrt{|\mu_+|} - i\sqrt{|\mu_-|}e^{2\pi i f \Delta t_d}, & y \le 1, \\ \sqrt{|\mu_+|}, & y \ge 1, \end{cases} \tag{5}$$

where $\mu_\pm$ and Δt_d are the magnification factors of two images and the time delay between them, respectively. $\mu_\pm$ and Δt_d are respectively given by

$$\mu_\pm = \frac{1}{2} \pm \frac{y^2+2}{2y\sqrt{y^2+4}}, \tag{6}$$

$$\Delta t_d = \frac{4GM_{Lz}}{c^3}\left[\frac{y\sqrt{y^2+4}}{2} + \ln\left\{\frac{\sqrt{y^2+4}+y}{\sqrt{y^2+4}-y}\right\}\right], \tag{7}$$

for the PM and

$$\mu_\pm = \pm 1 + \frac{1}{y}, \tag{8}$$

$$\Delta t_d = \frac{8GM_{Lz}y}{c^3}, \tag{9}$$

for the SIS. In Equations (7) and (9), $M_{Lz} = M_L(1+z_L)$ is the redshifted mass of a lens. From Equations (6) – (9), one can see that $\mu_\pm$ and Δt_d are given as the function of y and M_{Lz}. In this work, we regard y as free parameter and will discuss the constraint on the range of its value in the following section.

3. METHOD

3.1. *Data Preparation*

The main goal of this work is to identify lensed GWs with deep learning from the confirmed detections[1]. To this end, we describe the details of data preparation from the generation of simulated GWs to the preparation of practical spectrogram samples for the purpose.

3.1.1. *Gravitational-Wave Model*

We firstly consider a waveform model for GWs from the BBH. Specifically, we mainly focus on the inspiral phase instead of the merger and ringdown phases because the portion of the latter two phases are much shorter than inspiral phase to see the superposed waveform due to the two images of a lensed GW arrived at different time with Δt_d. In Singh et al. (2019), we have indeed shown that considering only the inspiral phase without the precision effect of the BBH system is sufficient to study the feasibility on the classification of lensed GWs from unlensed ones even in the pedagogical approach.

On the other hand, a precessing binary system originating from the non-zero and misaligned component spins can introduce modulation in the amplitude and phase of GWs (Hannam 2014) which may appear similar to the beating pattern of lensed GWs due to the superposition of two non-precessing GWs. Therefore, we also quantify our ability to discriminate lensed GWs from the precessing ones. However, in this work, we discard the lensing of precessing GWs for simplicity.

We use the IMRPhenomPv2 model (Schmidt et al. 2015; Hannam et al. 2014) for the generation of simulated waveforms of both non-precessing and precessing GWs in a consistent manner except the spin of component objects of the BBH merger. In the use of the waveform model, we set the range of the mass of individual component objects as $4M_\odot$ – $35M_\odot$ which is commonly used for the BBH merger in the conventional template-based GW data analysis methods such as `PyCBC` (Nitz et al. 2020; Usman et al. 2016) and `gstlal` (Sachdev et al. 2019; Messick et al. 2017). For the precessing GWs, we set the spin of the component objects as $s_1, s_2 \in [-1, 1]$.

3.1.2. *Constraint on Position Parameter*

Since we are interested in the lensing effect imprinted in GW which may appear as a beating pattern in a spectrogram, the order of time delay, Δt_d, between two images of a lensed

[1] See Figure 10 in Abbott et al. (2019) for the illustration of similar procedure using the standard nested sampling analysis.

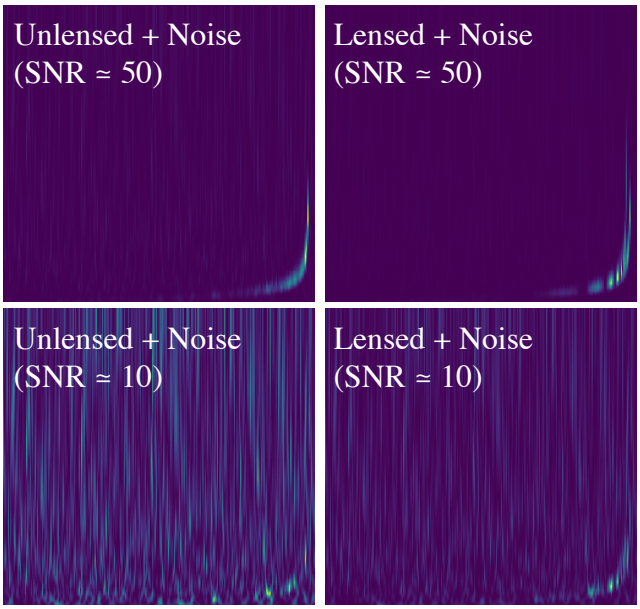

Figure 2. Example spectrograms of unlensed (left) and lensed (right) inspiral GWs of their optimal SNR $\simeq$ 50 (top) and $\simeq$ 10 (bottom) against a theoretical noise model of the Advanced LIGO. All chirp signals are generated by setting the same source component mass parameters, $m_1 = m_2 = 10M_\odot$ and $D_S = 2$ Gpc. For the generation of lensed cases (the right panels), we use the PM with setting $D_L = 1$ Gpc. With higher SNR, the gravitational lensing effect introduces an easily recognizable beating pattern and two peaks on the spectrogram of lensed signal, as shown in the top-right panel. However, with lower SNR (the bottom two panels), relatively higher noise strength which makes SNR to be lower and generates breaks on the spectrogram that looks like the beating pattern as shown in the bottom-left panel.

GWs is expected to be the order of millisecond. From Equations (7) and (9), we could see that Δt_d depends not only on M_L but also on y. Hence, we need to consider an appropriate range for y that can induce such amount of time delay. We can understand from Equation (5) that, when $y \geq 1$, $F(f)$ is determined by a single magnification factor, that is, only by μ_+ without μ_-. It means that only a single amplified image is formed around a lens for the case. Thus, in order to produce the observable beating pattern caused by two superposed images of a lensed GW, we limit the range of y to satisfy $0.05 < y < 1$ for both PM and SIS models.

3.1.3. *Preparation of Realistic Spectrogram Samples*

If there are negligible noises in a GW data containing a lensed GW, we may easily identify whether the detected GW is lensed or not (see examples in the top panels of Figure 2). However, in general, real GW data contains significant noises originating from various stationary and non-stationary noise sources which may hinder the identification (see examples in the bottom panels of Figure 2). Therefore, in order to study the capability of identifying lensed GW signal from noisy GW data, we need to prepare spectrograms which mimic realistic ones as much as possible.

Table 1. Ranges for the randomized parameters of the lensed GWs. The range of SNR is used for the criterion of taking or discarding generated samples with the randomized parameters. The range of component spins is applied for x-, y-, and z-directions individually. Note that the source and lens masses are sampled from a logarithmic distribution to reduce the bias towards more heavily lensed waveforms being generated.

Parameter	Range
Component masses of source, m_1 & m_2	$4 - 35M_\odot$
Lens mass, M_L	$10^3 - 10^5 M_\odot$
Distance to lens, D_L	$10 - 10^3$ Mpc
Distance from lens to source, D_{LS}	$10 - 10^3$ Mpc
Displacement of source from the line of sight, γ	0 – 0.5 pc
Redshift, z	0 – 2
Signal-to-noise ratio, SNR	10 – 50
Component spins, s_1 & s_2	[-1, 1]

For the preparation of realistic noise data, we adopt the PSD of a theoretical noise model, Detuned High Power model of the Advanced LIGO (Shoemaker 2009), which can be obtained from running `PyCBC`. We add the noise data to the simulated signals described in the previous section.

We then conduct a selection procedure on the noise added signal samples based on their SNR[2]; taking only samples satisfying a condition, $10 \leq$ SNR ≤ 50, that covers the SNRs of the 10 BBH-GWs reported in the GWTC-1. For the selected samples, we finally apply a conventional time-frequency representation called the constant-Q transform (Chatterji et al. 2004) to generate our spectrogram samples.

In Table 1, we summarize the parameters used in the preparation of the final form of spectrogram samples reflecting the considerations and constraints discussed in the previous sections. The number of resulting spectrogram samples is 45,000 for each of (i) lensed (L), (ii) unlensed and non-precsseing (U_N), and (iii) unlensed and precessing (U_P) GWs.

3.2. *Application of Deep Learning*

In this section, we present a brief introduction of the deep learning model adopted in this work and the detailed procedure of training the deep learning model.

3.2.1. *Visual Geometry Group Network*

[2] The SNR computed in this work is the optimal SNR because the noise and the exact form of GW signal are known (Creighton & Anderson 2011).

The network structure of the VGG has been designed as a variant of the classical type of convolutional neural networks which is inspired by the AlexNet (Krizhevsky et al. 2012). The main insight of the VGG is using only 3x3 convolutional filters in the construction of deeper networks.[3]

For the classification and regression of our interest, we use the latest version of the VGG, VGG-19, and implement it with `PyTorch` (Paszke et al. 2019). We summarize the structural details used for the implementation of VGG-19 in Appendix A. Henceforth we refer the VGG-19 as VGG for convenience.

3.2.2. *Input Data*

For the application of the VGG to the spectrogram samples prepared in Section 3.1.3, we split the samples into three subset data such as training, validation, and evaluation data. We randomly choose 80% of total samples for the training data and 10% each for the validation and evaluation data.

We then perform a preprocessing, the min-max normalization, on the samples in all subsets by rescaling the values of pixels in a spectrogram sample to be normalized between -1 and 1. It is known that this kind of preprocessing helps mitigating the vanishing gradient problem (Hochreiter et al. 2001) which could be occurred in the training. Another benefit of this preprocessing is that we can keep the information of SNR of an original sample even with the normalization. We use each of the preprocessed subset data as the input data which are fed into each step of training, validation, and evaluation, respectively.

Meanwhile, particularly for the regression, we prepare additional data called target data with the parameters to be predicted by the VGG on top of the spectrogram samples. For the parameters, we consider y, μ_+, μ_-, M_S^c, M_L, z_S, and z_L. We normalize each of the parameters with the min-max normalization too since (i) the ranges of parameters to be predicted by the VGG are quite different as shown in Table 1 and (ii) diversely ranged target data may cause biased results. Consequently, we can restrict the contribution of each target value into a comparable range and may avoid the diversely ranged target parameters contributing differently to the loss function that will be discussed in Section 3.2.4. However, for the final estimation of the values of the parameters, we conduct a postprocessing on the predicted outputs by reversely performing the min-max normalization to recover their original value.

3.2.3. *Training VGG*

[3] There is a competitive model called Inception (Szegedy et al. 2014, 2015, 2016) also known as GoogLeNet. But, it is shown that the VGG is more robuster for the face recognition in the presence of noise than Inception (Grm et al. 2018). Thus, we decide to use VGG since we are also interested in recognizing lensed GW signals from the presence of noise,

Table 2. The training setup of the VGG model. We employ the configurations for both classification and regression.

Parameter	Value
Batch size	128
Maximum training epoch	100
Optimization algorithm	Adam
Learning rate decay strategy	On plateau
Initial learning rate	8e-5
Minimum learning rate	1e-5
Decay factor	2
Computing processor	NVIDIA Tesla P40 (24GB)

We train the VGG with the training data by setting a batch size to be 128 for both classification and regression. The maximum training epoch is set as 100 while iterating whole samples in the training data. To boost the training and enhance the accuracy of the VGG, we use the Adam optimization algorithm (Kingma & Ba 2014), one of extensions of the stochastic gradient descent method. For the implementation of the learning rate decay, we reduce the learning rate by a factor of 2 from the initial learning rate when the training stops updating the VGG since it is known that most of deep learning models often get benefit from the reduction of learning rate.

During the training, we keep tracking the validity of a temporal model at each epoch and save a checkpoint for the temporal model to check improvement compared to the former best performing model on the same validation data. The VGG is trained on NVIDIA Tesla P40 GPU with 24GB memory. In Table 2 we summarize the parameters and criterion methods that we used.

We identically apply this setup for both classification and regression. However we alter the form of output for each task such that let the classification return the probability to each sample type either U_N, U_P, or L via the one-hot encoding and let the regression return the normalized value of parameters via the $\tanh$ function because we use the normalized target data.

3.2.4. *Error Measurement in Training*

The successful training of the VGG relies on whether the final output of the model returns the most closest probability to the given type of GW, e.g., either lensed or unlensed signals in classification or the most closest value to the target value in regression. In other words, we need to deploy an adequate error measurement method, E, (or, equivalently, loss function) to let the VGG can be properly updated through multiple iterations and, eventually, let it can return desired output within acceptable tolerance on the error.

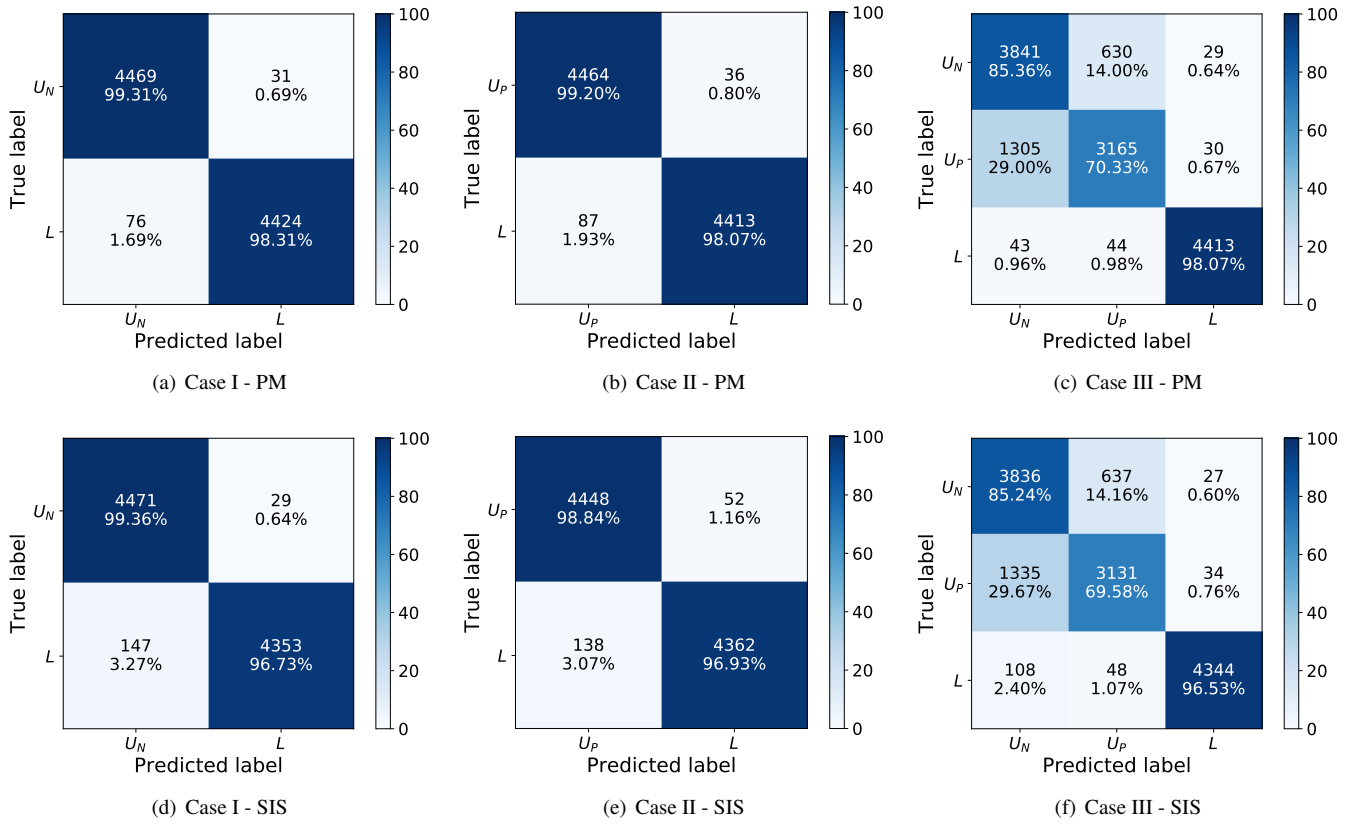

(a) Case I - PM (b) Case II - PM (c) Case III - PM

(d) Case I - SIS (e) Case II - SIS (f) Case III - SIS

Figure 3. Confusion matrices for the classification on U_N vs. L (Case I), U_P vs. L (Case II), and U_N vs. U_P vs. L (Case III) from the left to the right, respectively. The colorbar indicates the ratio of correctly or incorrectly classified samples to the total number of samples of each signal type. The diagonal and off-diagonal cells respectively show correctly classified and misclassified samples. The number of classified samples is given in the middle of each cell followed by the ratio of the samples in percentage to the total number of true samples.

We use different forms of loss functions for the classification and regression separately. We compute the cross-entropy function:

$$E_{\rm c} = -p_i \log \hat{p}_i, \tag{10}$$

for the classification at each iteration of training until the value of $E_{\rm c}$ satisfies given tolerance for the error. In Equation (10), $\hat{p}_i$ and p_i are the predicted value and the target value of an i-th training sample. Meanwhile, for the regression, we measure E with mean squared error:

$$E_{\rm r} = \frac{1}{N}\sum_{i}^{N}(\hat{p}_i - p_i)^2, \tag{11}$$

where N is the total number of training samples.

4. RESULTS

4.1. *Classification*

For the evaluation of classification performance, we firstly investigate how much the trained VGG correctly distinguishes the spectrograms of L from U_N (Case I) or from U_P (Case II). Next, we study the ability on the discrimination of all of three different types, L, U_N, and U_P (Case III). We separate L further into $L_{\rm PM}$ and $L_{\rm SIS}$ depending on the lens model. We calculate the confusion matrix for a figure-of-merit of classification performance and present it in Figure 3 with the number and ratio of correctly and incorrectly classified samples.

In the comparison between $L_{\rm PM}$ and $L_{\rm SIS}$ (see the bottom-right cells in Figures 3), we can see that $\sim 98\%$ of $L_{\rm PM}$ samples are correctly classified while $\sim 97\%$ of $L_{\rm SIS}$ samples are correctly classified. We seek a reason of the small difference from the distribution of probability density function (PDF) of correctly and incorrectly classified samples drawn with respect to their SNRs (Figure 4). We can see from Figure 4 that the difference between the mean SNRs of correctly classified and incorrectly classified $L_{\rm PM}$ samples are relatively larger than $L_{\rm SIS}$ samples in both Case I and II. It means that the beating pattern of $L_{\rm SIS}$ samples might be slightly less distinguishable from U_N or U_P than $L_{\rm PM}$ samples even with higher SNRs. From this observation we can see that when the beating pattern is insignificant the classification performance of the VGG is certainly limited. We also found that the SNR distribution is consistent to the result of confusion matrix too.

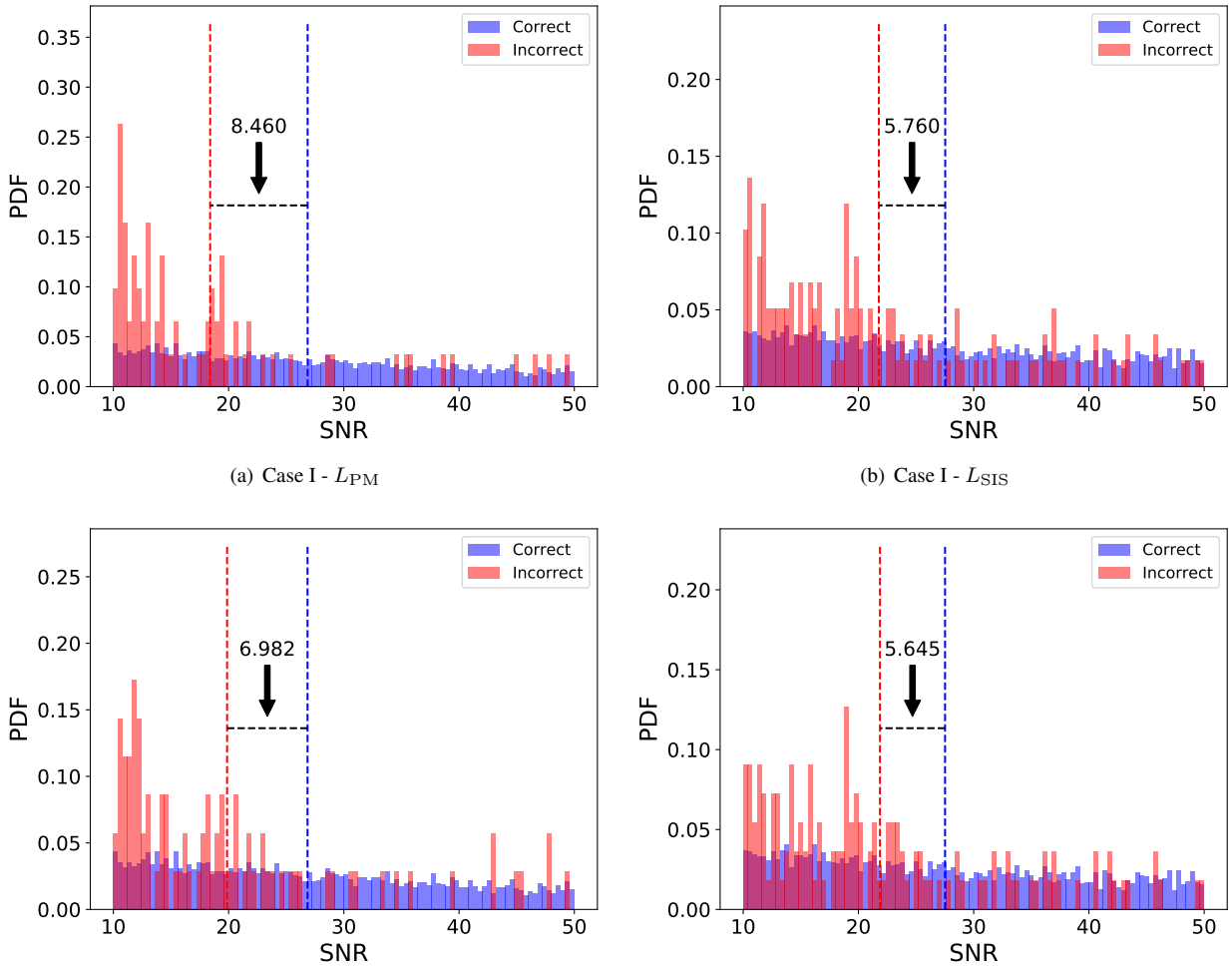

(a) Case I - $L_{\rm PM}$ (b) Case I - $L_{\rm SIS}$

(c) Case II - $L_{\rm PM}$ (d) Case II - $L_{\rm SIS}$

Figure 4. The distribution of PDF with respect to the SNRs of each sample type. For either U_N or U_P, compared lens model is presented in the subscription. The PDF of correctly classified samples is presented by the blue-bars and that of incorrectly classified ones is presented by the red-bars. The blue and red dashed-lines indicate the mean values of correctly classified and incorrectly classified samples, respectively, and the difference between the mean SNR values are annotated as the number.

The trained VGGs of both Case I and II can correctly classify expected types over 96% of the evaluation data as shown in the diagonal cells of the left and middle panels of Figure 3. When we look at the spectrogram examples of correctly classified and incorrectly classified samples from Figure 5, we can see that correctly classified samples of $L_{\rm PM}$ and $L_{\rm SIS}$ show clearer beating patterns distinguishable from U_N or U_P (see the first and third rows of Figure 5). However, as shown in the second and fourth rows of Figure 5, the beating pattern of incorrectly classified $L_{\rm PM}$ and $L_{\rm SIS}$ samples are not remarkably distinguishable from U_N or U_P even for higher SNRs $\gtrsim 30$. For those incorrectly classified L samples, we suspect that Δt_d is too short to generate visibly significant beating pattern. As an evidence for the suspicion, we investigate the distribution of Δt_d for the L samples corresponding to SNR ~ 30 (see Figure 6) and see that the L samples generated with the random parameters resulting in $\Delta t_d < 0.25$ sec are mostly misclassified.

Meanwhile, for the Case III (the right panels in Figure 3), when we compare the confusion matrices to those of Case I and II, the ratios of correctly classified samples are similar to or slightly decreased than Case I and II. Particularly, the ratio of correctly classified samples is significantly decreased by $\sim 14\%$ for the U_N and $\sim 28\%$ – 29% for the U_P while it is decreased by only $\lesssim 0.4\%$ for the L. From this result we can see that the beating pattern caused by the lensed GWs is still sufficiently significant than the unlensed ones either U_N or U_P. In the meantime, from the comparison between U_N and U_P in the Case III, we see that $\sim 14\%$ – 29% of samples are misclassified, that is, classified U_N as U_P or vice versa. Especially, the ratio of U_P to U_N is $\gtrsim 15\%$ higher than the opposite case. We suppose a reason of this result that, as shown in Figure 5, the effect of modulation occurred by the

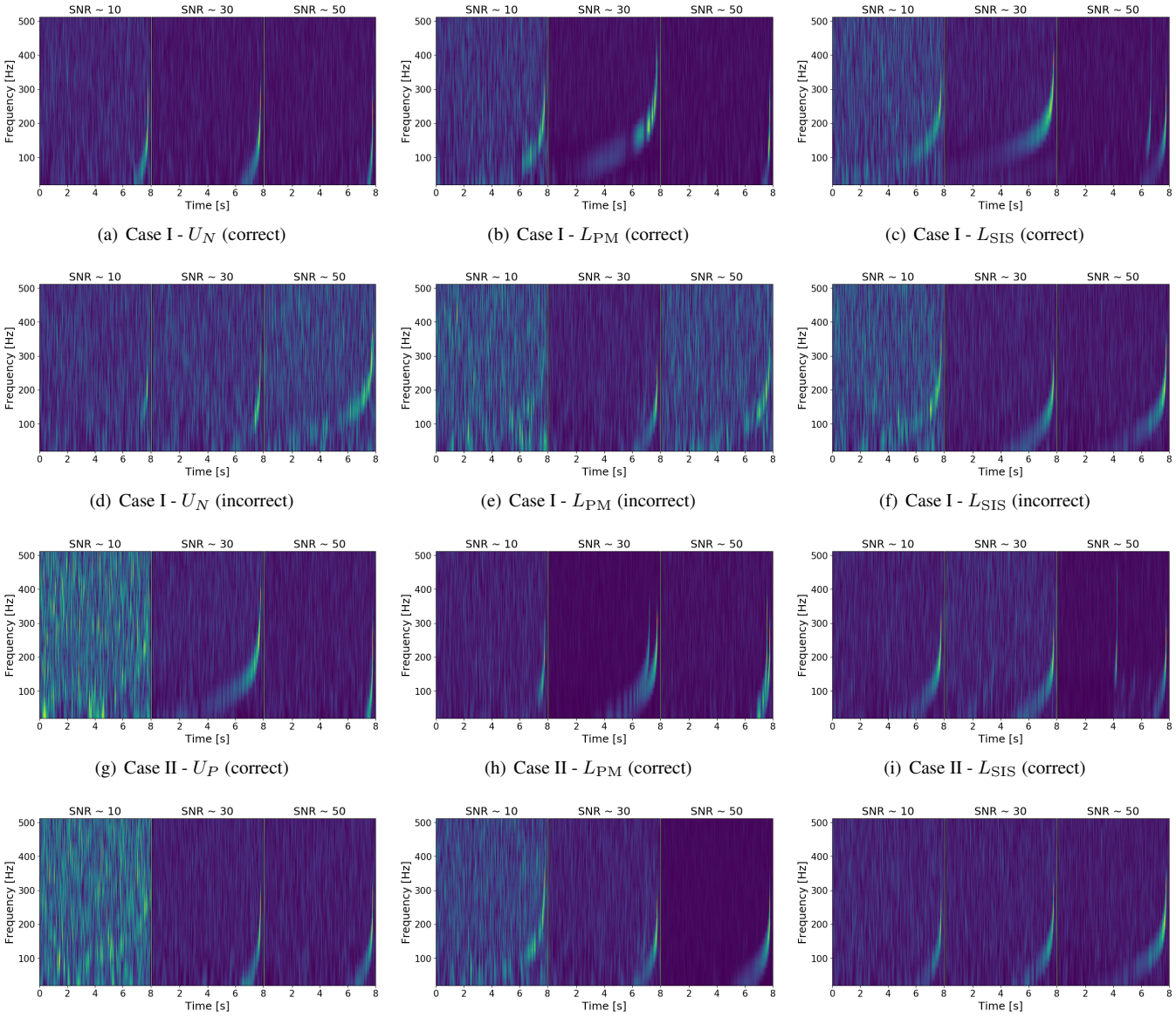

(a) Case I - U_N (correct) (b) Case I - $L_{\rm PM}$ (correct) (c) Case I - $L_{\rm SIS}$ (correct)

(d) Case I - U_N (incorrect) (e) Case I - $L_{\rm PM}$ (incorrect) (f) Case I - $L_{\rm SIS}$ (incorrect)

(g) Case II - U_P (correct) (h) Case II - $L_{\rm PM}$ (correct) (i) Case II - $L_{\rm SIS}$ (correct)

(j) Case II - U_P (incorrect) (k) Case II - $L_{\rm PM}$ (incorrect) (l) Case II - $L_{\rm SIS}$ (incorrect)

Figure 5. Spectrogram examples of correctly and incorrectly classified from Case I (the first and second rows, respectively) and Case II (the third and fourth rows, respectively). Each subfigure consists of three spectrograms of SNR $\sim 10, 30, 50$ from the left to the right, respectively. We can see from the panels in the second and fourth rows that, if Δt_d is too short, the spectrograms of $L_{\rm PM}$ and $L_{\rm SIS}$ look similar to U_N and incorrectly classified even for higher SNRs $\gtrsim 30$.

precession is less significant to produce remarkable pattern like the beating pattern of L.

4.2. *Regression*

For the regression on the characteristic parameters of lensed GWs, we have trained VGG in Section 3.2.3 to predict the 7 selected parameters, y, μ_+, μ_-, M_S^c, M_L, z_S, and z_L. Note that we introduce the chirp mass of a source binary, $M_S^c = (m_1 m_2)^{2/5}(m_1+m_2)^{-1/5}$, because it is a convenient parameter in describing the characteristics of the evolution of GW waveform (Abbott et al. 2016). Among the 7 parameters, we consider $\mu_\pm$ as optional parameters to check the sanity of the predicted y since $\mu_\pm$ are written as the function of y as shown in Equations (6) and (8). Also we consider the redshift factors, z_S and z_L, instead of the distances, D_S and D_L, because Δt_d depends not only on y but on M_{Lz}. For the conversion of the distances to the redshift factors, we suppose that the Hubble constant is $70\ {\rm km}\cdot{\rm s}^{-1}\cdot{\rm Mpc}^{-1}$.

We examine the performance of regression on the evaluation data by comparing the predicted parameters to the true parameters. The results are shown in Figures 7 and 8. For the figures, note that if the regression works ideally, we expect all

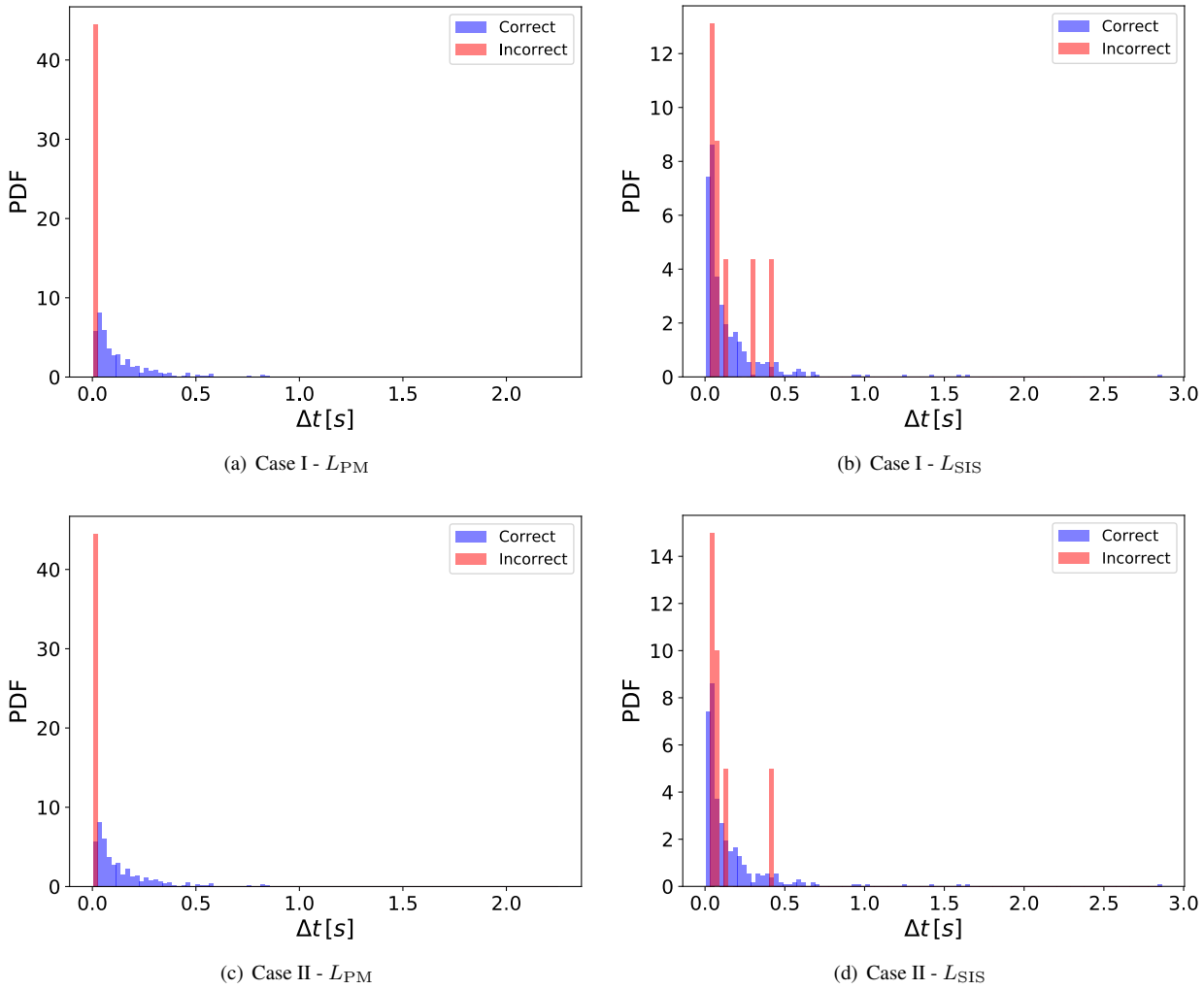

(a) Case I - $L_{\rm PM}$ (b) Case I - $L_{\rm SIS}$

(c) Case II - $L_{\rm PM}$ (d) Case II - $L_{\rm SIS}$

Figure 6. The distribution of PDF with respect to Δt_d of each sample type corresponding to SNR $\sim$ 30. The color-bar represents the same cases, correctly classified (blue) and incorrectly classified (red) samples as presented in Figure 4.

of predicted values are placed on the black dashed-line. In addition to the comparison figure, for the quantitative measure of the performance, we consider two metrics: the mean residual,

$$R := \frac{1}{N_{\hat{p}}} \sum_{\hat{p}} \frac{|\hat{p} - p|}{p + 1}, \tag{12}$$

and the Bhattacharyya distance (Bhattacharya 1943),

$$D_{\rm B} := -\ln(\sum_{\hat{p}} \sqrt{P(\hat{p})P(p)}). \tag{13}$$

R describes how much predicted values are different from true values. $D_{\rm B}$ describes the similarity between the probability distribution of predicted values and the probability distribution of true ones.

As shown in the left panels of Figure 7, it is visible that the distribution of predicted y at $y \simeq 1$ is relatively narrower than $y \ll 1$ for both PM and SIS. One can also see that, as the value of y decreases, the distribution becomes broader while more points are in the upper triangle region than the lower one. This result means the predicted values of y are rather overestimated where $y \ll 1$. On the other hand, when we compare the results of prediction on $\mu_{\pm}$ (the middle and right panels of Figure 7 to y, it looks that the distribution of predicted $\mu_{\pm}$ agrees with Equations (6) and (8) as expected.

Next, in the comparison between the PM and SIS, we see that the distribution of the predicted y of SIS is more confined to the black dashed-line than PM. It is also shown in the quantitative metrics, R and D_B: As tabulated in Table 3, the values of $R_{\rm SIS}$ and $D_{\rm B,SIS}$ are smaller than $R_{\rm PM}$ and $D_{\rm B,PM}$, respectively. Thus, it seems that R is better metric in obtaining consistent results.

We also present the regression results of other parameters in Figure 8 and Table 4. From the figure, we can see that the regressions of the parameters related to the source are better than those of the lens, that is, the predicted values of M_S^c and z_S are distributed more closer to the the black dashed line

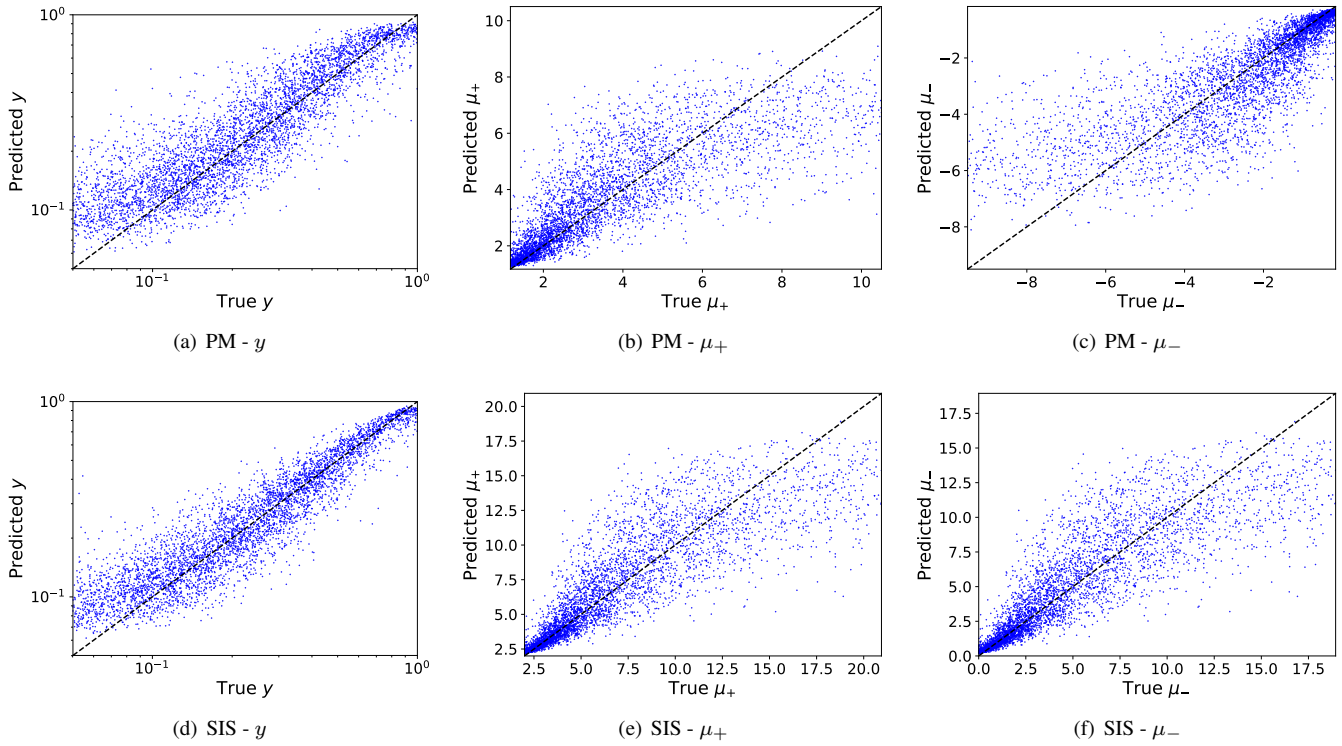

(a) PM - y (b) PM - μ_+ (c) PM - μ_-

(d) SIS - y (e) SIS - μ_+ (f) SIS - μ_-

Figure 7. Comparison of predicted and true parameters of y and $\mu_\pm$. The x-axes indicate true parameters used for the generation of $L_{\rm PM}$ or $L_{\rm SIS}$ and the y-axes indicate predicted parameters from the regression. One can see that the distribution of predicted values of $\mu_\pm$ seems consistent with that of y as expected from Equations (6) and (8).

Table 3. R and $D_{\rm B}$ of the regression results of y and $\mu_\pm$. The bold-faced values show better result in the comparison between the PM and SIS.

Metric and Lens Model	y	μ_+	μ_-
$R_{\rm PM}$	0.0531	0.1737	2.1666
$R_{\rm SIS}$	**0.0380**	**0.1660**	**0.2440**
$D_{\rm B,PM}$	0.0385	0.0568	0.0567
$D_{\rm B,SIS}$	**0.0345**	**0.0500**	**0.0499**

than those of M_L and z_L. Also, from the table, we see that Rs and $D_{\rm B}$s of the source related parameters are smaller than those of the lens.

Meanwhile, in the comparison between PM and SIS, we see that both R and $D_{\rm B}$ are mostly consistent with the visually recognizable distributions shown in Figure 8. However, when we look at M_S^c and M_L, the result of R is more consistent with the comparison figures than D_B. So, we conclude that R is more suitable metric than D_B for the quantitative measure on the regression of this work based on the consistency between the comparison figure and the metric.

However, we know that the characteristics of lens are highly degenerated; for example, y is characterized not only by γ, D_L, ξ, and D_{LS} explicitly but also by M_L implicitly which make the uncertainties of each parameter to be mixed in a single parameter y while the characteristics of the GWs from the BBH have relatively less degeneracy because we only need to consider the uncertainties on M_S^c and D_S. Thus, we conclude that the amount of uncertainty might lead the limitation in precisely estimating the uncertain and degenerated characteristics of the lens from the beating pattern only.

5. DISCUSSION

In this work, we considered the range of the mass of lens as $10^3 M_\odot - 10^5 M_\odot$. The mass range is much smaller than the known masses of galaxies that cover from $\sim 10^9 M_\odot$ (dwaft galaxy) to $\sim 10^{12} M_\odot$ (giant galaxy) which can observed in the ground-based GW detectors as repeated events. Instead, the chosen mass range may correspond to the mass range of certain astrophysical compact objects such as intermediate mass black holes (Greene et al. 2019) or compact dark matter (Jung & Shin 2019). Thus, if we can identify lensed GWs occurred by the lens system discussed in this work, the identification may help to understand the characteristics of such compact objects.

We have discarded the lensing of precessing GWs to simplify the problem. However, as shown in the classification of Case II, precessing effect itself is mostly distinguishable from the lensed GWs while it is less distinguishable than non-precessing GWs in the classification of Case III. Since it

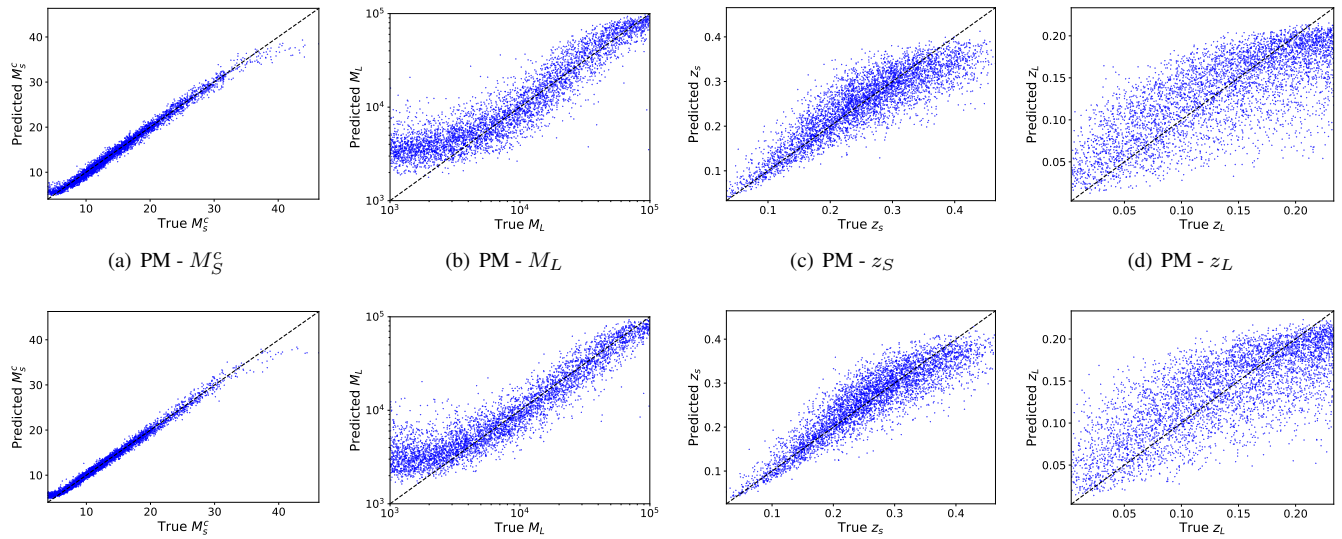

(a) PM - M_S^c (b) PM - M_L (c) PM - z_S (d) PM - z_L

(e) SIS - M_S^c (f) SIS - M_L (g) SIS - z_S (h) SIS - z_L

Figure 8. Comparison of predicted and true parameters of $M_{\rm S}^c$, $M_{\rm L}$, $z_{\rm S}$, and $z_{\rm L}$. The units of M_S^c and M_L are given in $M_\odot$.

Table 4. R and $D_{\rm B}$ of the regression results of M_S, M_L, z_S, and z_L. The bold faced values show better result in the comparison between PM and SIS while the asterisk in the superscript show better one in the comparison between the source and lens.

Metric and Lens Model	M_S^c	M_L	z_S	z_L
$R_{\rm PM}$	0.0442*	0.6035	0.0262*	0.0285
$R_{\rm SIS}$	**0.0391***	**0.5274**	**0.0231***	**0.0281**
$D_{\rm B,PM}$	**0.0077***	**0.1030**	0.0288*	0.0517
$D_{\rm B,SIS}$	0.0083*	0.1071	**0.0176***	**0.0447**

is expected that the lensing effect not only introduce the beating pattern but also does amplify the original waveform, we may expect that lensing of precessing GWs can increase the significance of precessing GWs even for the Case III. Therefore, to extract the lensing signature from this case, further systematic study about the effect of lensing parameters on the lensed precessing GWs should be done along with the identification.

As seen from the result of regression, the uncertainty in the prediction on the characteristic parameters related to the lens was much larger than that on the parameters related to the source. In other words, we may conclude that the degenerated information contained in the spectrogram is not sufficient to fully characterize the lens. For this issue, we believe that additional information obtained from the EM observations will be helpful in reducing the uncertainty and, consequently, in enhancing the prediction power of the regression about the lens. For example, for a lensed GW, we may conduct more finer estimation on the physical parameters of the lens by finding coincident lensing events in the optical band survey with the LSST[4] (Abell et al. 2009). Meanwhile, for the lens system like galaxy or galaxy cluster, we may understand more details of physical properties of the lens by the near-infrared observation with the SPHEREx[5] (Doré et al. 2016). Therefore, we expect that the identification of lensed GWs will be one of exciting fields where the multimessenger observations will be definitely impactful.

On the other hand, within the sensitive frequency band of Advanced LIGO and Virgo, the possibility of observing GWs lensed by the microlenses embedded in a galaxy or galaxy cluster is discussed in Diego et al. (2019) and Pagano et al. (2020). For example, it is shown that the evolution of $F(f)$ of this scenario will be non-negligible (see Figure 6 of Pagano et al. (2020)) and GWs lensed by the microlenses around such macrolens systems can be observed (see Figure 10 of Pagano et al. (2020)). In consequence, we can seamlessly anticipate to see recognizable beating pattern from the spectrogram for the scenario too. As an example, we simply evaluate a spectrogram sample prepared by using `lensingGW` package (Pagano et al. 2020; Birrer & Amara 2018). The strain of this test and its spectrogram sample are presented in Figure 9 and the parameters used for generating this sample are summarized in Appendix B. For the evaluation we use the VGGs of PM and SIS lens models (VGG-PM and VGG-SIS respectively) trained for the classification of Case I. As the result, the VGG-SIS correctly classifies this sample with 100% accuracy to L while the VGG-PM incorrectly classifies this

[4] Large Synoptic Survey Telescope (Ivezić et al. 2019). Recently the name has been changed to Vera C. Rubin Observatory.

[5] Spectro-Photometer for the History of the Universe, Epoch of Reionization, and Ices Explorer (Korngut et al. 2018)

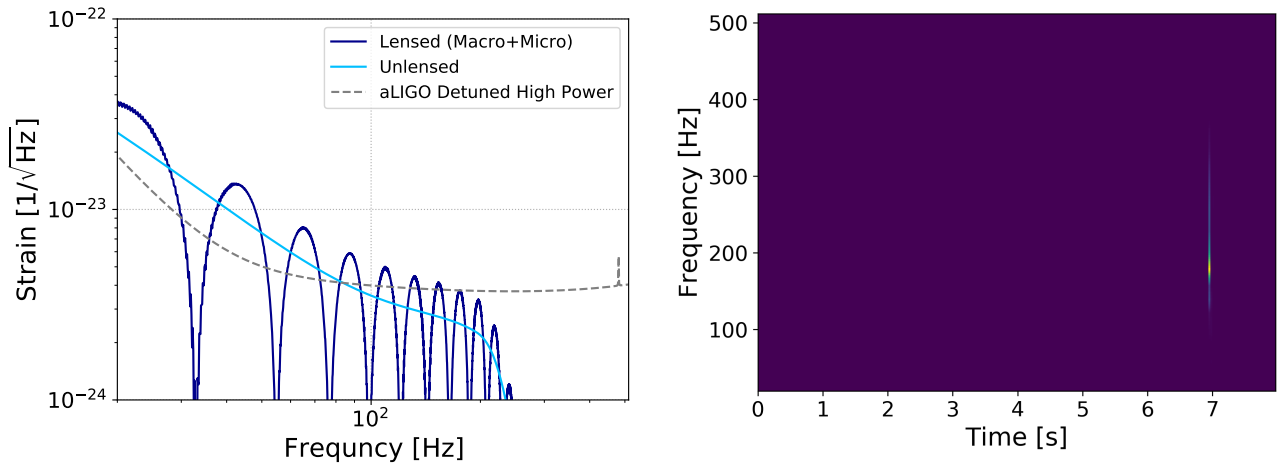

(a) Strain

(b) Spectrogram

Figure 9. Strain of a microlensed GW (left) and its spectrogram (right) generated with the parameters and tools summarized in Appendix B.

sample with 37% accuracy to L. Therefore, we can ascertain from this test that there is plentiful prospect for increasing the performance of the identification of the microlensing signature from spectrograms even with more complicated lens models. To do that, we can train the VGG with a new training set of data prepared by using the `lensingGW` package. However, we leave the full application of our method to the search of microlensing in GWs to the future work.

ACKNOWLEDGMENTS

We thank Giulia Pagano for useful discussion in the use of `lensingGW`. We also thank the Global Science experimental Data hub Center (GSDC) at KISTI for supporting GPU-based computing resource. KK is supported by the National Research Foundation of Korea (NRF) grant funded by the Korea government (MSIT) (NRF-2020R1C1C1005863). OAH is supported by the research program of the Netherlands Organization for Scientific Research (NWO). TGFL is partially supported by grants from the Research Grants Council of Hong Kong (Project No. 14306218), Research Committee of the Chinese University of Hong Kong, and the Croucher Foundation of Hong Kong.

APPENDIX

A. DETAILS OF IMPLEMENTED VGG

We use 10 convolutional layers which consist of 3x3 convolutional filters. The number of filters in order are [16, 16, 16, 32, 32, 32, 64, 64, 64, 64, 64, 128, 128, 128, 128, 128, 128, 128, 128, 128, 128]. The strides for each convolutional layers are [1x1, 1x1, 2x2, 1x1, 1x1, 2x2, 1x1, 1x1, 1x1, 1x1, 2x2, 1x1, 1x1, 1x1, 1x1, 2x2, 1x1, 1x1, 1x1, 1x1, 2x2]. Note that, unlike the structure of the original VGG-19 model, no pooling layers are used in this work since pooling layers are known to cause information losses in the forward propagation of the network (Springenberg et al. 2014) which are not desirable for the regression problem. Instead, the functionality of pooling layers are replaced by the strides.

For the activation function between adjacent convolutional layers, *exponential linear unit* function is used, while *softmax* (classification) and *hyperbolic tangent* (regression) activations are used for the fully connected part of the network. Dropout rate between layers is set as 0.01.

B. DETAILS OF MICROLENSING SAMPLE

For the use of `lensingGW` in preparing a sample spectrogram of microlensed GW, we consider a simple case similar to the case discussed in Sec. 5.2. of Pagano et al. (2020), that is, the microlensing of GWs enhanced by a macrolens like elliptic galaxy. We consider to set the parameters rather differently and arbitrarily such as $m_1 = 45M_\odot$, $m_2 = 36M_\odot$, $M_L = 10^{12}M_\odot$, $z_S = 0.2$, and $z_L = 0.05$. With this setup, we get $\theta_E = 2.65 \times 10^{-5}$ radian. The sky position (RA, Dec) of a source binary

system is set as $(0.05, 0)\theta_E$ radian. The generation of an unlensed and non-precessing GW is done by using IMRPhenomPv2. For the distribution of microlenses, we assume that the point masses are distributed uniformly within the range of $[100, 200]M_\odot$ and their positions are uniformly distributed within $\pm 10^{-4}\times$(RA, Dec) around the (RA, Dec) of a chosen macro image. For this setup, `lensingGW` solver found 138 microlensed images. Finally we convert the strain data into the spectrogram via the constant-Q transform method as done in this work. Because the setup is just prepared for testing and piloting purposes, we take a very high SNR $\simeq 63$.

REFERENCES

Aasi, J., et al. 2015, Class. Quant. Grav., 32, 074001, doi: 10.1088/0264-9381/32/7/074001

Abbott, B. P., et al. 2016, Phys. Rev. Lett., 116, 061102, doi: 10.1103/PhysRevLett.116.061102

—. 2019, Phys. Rev. X, 9, 031040, doi: 10.1103/PhysRevX.9.031040

Abell, P. A., Allison, J., Anderson, S. F., et al. 2009, LSST Science Book, Version 2.0. https://arxiv.org/abs/0912.0201

Acernese, F., et al. 2015, Class. Quant. Grav., 32, 024001, doi: 10.1088/0264-9381/32/2/024001

Bhattacharya, A. K. 1943, Bull. Calcutta Math. Soc., 35, 99

Birrer, S., & Amara, A. 2018, Physics of the Dark Universe, 22, 189, doi: 10.1016/j.dark.2018.11.002

Bliokh, P. V., & Minakov, A. A. 1975, Ap&SS, 34, L7, doi: 10.1007/BF00644818

Bontz, R. J., & Haugan, M. P. 1981, Ap&SS, 78, 199, doi: 10.1007/BF00654034

Cassan, A., Kubas, D., Beaulieu, J.-P., et al. 2012, Nature, 481, 167

Chatterji, S., Blackburn, L., Martin, G., & Katsavounidis, E. 2004, Class. Quant. Grav., 21, S1809, doi: 10.1088/0264-9381/21/20/024

Clowe, D., Gonzalez, A., & Markevitch, M. 2004, The Astrophysical Journal, 604, 596

Creighton, J. D. E., & Anderson, W. G. 2011, Gravitational-Wave Data Analysis (John Wiley & Sons, Ltd), 269–347, doi: 10.1002/9783527636037.ch7

Dai, L., Li, S.-S., Zackay, B., Mao, S., & Lu, Y. 2018, Physical Review D, 98, 104029

Dai, L., Zackay, B., Venumadhav, T., Roulet, J., & Zaldarriaga, M. 2020. https://arxiv.org/abs/2007.12709

Deguchi, S., & Watson, W. D. 1986, ApJ, 307, 30, doi: 10.1086/164389

Diego, J., Hannuksela, O., Kelly, P., et al. 2019, Astron. Astrophys., 627, A130, doi: 10.1051/0004-6361/201935490

Doré, O., Werner, M. W., Ashby, M., et al. 2016, Science Impacts of the SPHEREx All-Sky Optical to Near-Infrared Spectral Survey: Report of a Community Workshop Examining Extragalactic, Galactic, Stellar and Planetary Science. https://arxiv.org/abs/1606.07039

Greene, J. E., Strader, J., & Ho, L. C. 2019, arXiv e-prints, arXiv:1911.09678. https://arxiv.org/abs/1911.09678

Grm, K., Štruc, V., Artiges, A., Caron, M., & Ekenel, H. K. 2018, IET Biometrics, 7, 81–89, doi: 10.1049/iet-bmt.2017.0083

Hannam, M. 2014, Gen. Rel. Grav., 46, 1767, doi: 10.1007/s10714-014-1767-2

Hannam, M., Schmidt, P., Bohé, A., et al. 2014, Phys. Rev. Lett., 113, 151101, doi: 10.1103/PhysRevLett.113.151101

Hannuksela, O., Haris, K., Ng, K., et al. 2019, Astrophys. J. Lett., 874, L2, doi: 10.3847/2041-8213/ab0c0f

Hannuksela, O. A., Collett, T. E., Çalı şkan, M., & Li, T. G. 2020, doi: 10.1093/mnras/staa2577

Haris, K., Mehta, A. K., Kumar, S., Venumadhav, T., & Ajith, P. 2018, ArXiv e-prints. https://arxiv.org/abs/1807.07062

Hochreiter, S., Bengio, Y., Frasconi, P., & Schmidhuber, J. 2001, in A Field Guide to Dynamical Recurrent Neural Networks, ed. S. C. Kremer & J. F. Kolen (IEEE Press), 237–244

Ivezić, v. Z., et al. 2019, Astrophys. J., 873, 111, doi: 10.3847/1538-4357/ab042c

Jung, S., & Shin, C. S. 2019, Phys. Rev. Lett., 122, 041103, doi: 10.1103/PhysRevLett.122.041103

Kingma, D., & Ba, J. 2014, International Conference on Learning Representations

Korngut, P. M., Bock, J. J., Akeson, R., et al. 2018, in Space Telescopes and Instrumentation 2018: Optical, Infrared, and Millimeter Wave, ed. M. Lystrup, H. A. MacEwen, G. G. Fazio, N. Batalha, N. Siegler, & E. C. Tong, Vol. 10698, International Society for Optics and Photonics (SPIE), 576 – 586, doi: 10.1117/12.2312860

Krizhevsky, A., Sutskever, I., & Hinton, G. E. 2012, in Advances in Neural Information Processing Systems 25, ed. F. Pereira, C. J. C. Burges, L. Bottou, & K. Q. Weinberger (Curran Associates, Inc.), 1097–1105. http://papers.nips.cc/paper/4824-imagenet-classification-with-deep-convolutional-neural-networks

Lai, K.-H., Hannuksela, O. A., Herrera-Martín, A., et al. 2018, Phys. Rev. D, 98, 083005, doi: 10.1103/PhysRevD.98.083005

Li, A. K., Lo, R. K., Sachdev, S., et al. 2019. https://arxiv.org/abs/1904.06020

Li, S.-S., Mao, S., Zhao, Y., & Lu, Y. 2018, Monthly Notices of the Royal Astronomical Society, 476, 2220

Markevitch, M., Gonzalez, A., Clowe, D., et al. 2004, The Astrophysical Journal, 606, 819

McIsaac, C., Keitel, D., Collett, T., et al. 2019. https://arxiv.org/abs/1912.05389

Messick, C., et al. 2017, Phys. Rev. D, 95, 042001, doi: 10.1103/PhysRevD.95.042001

Nakamura, T. T. 1998, Phys. Rev. Lett., 80, 1138, doi: 10.1103/PhysRevLett.80.1138

Nakamura, T. T., & Deguchi, S. 1999, Prog. Theor. Phys. Suppl., 133, 137, doi: 10.1143/PTPS.133.137

Ng, K. K. Y., Wong, K. W. K., Broadhurst, T., & Li, T. G. F. 2018, Phys. Rev. D, 97, 023012, doi: 10.1103/PhysRevD.97.023012

Nitz, A., Harry, I., Brown, D., et al. 2020, gwastro/pycbc: PyCBC release v1.16.11, v1.16.11, Zenodo, doi: 10.5281/zenodo.4075326

Oguri, M. 2018, Mon. Not. Roy. Astron. Soc., 480, 3842, doi: 10.1093/mnras/sty2145

Ohanian, H. C. 1974, Int. J. Theor. Phys., 9, 425, doi: 10.1007/BF01810927

Pagano, G., Hannuksela, O. A., & Li, T. G. 2020. https://arxiv.org/abs/2006.12879

Pang, P. T., Hannuksela, O. A., Dietrich, T., Pagano, G., & Harry, I. W. 2020, doi: 10.1093/mnras/staa1430

Paszke, A., Gross, S., Massa, F., et al. 2019, in Advances in Neural Information Processing Systems 32, ed. H. Wallach and H. Larochelle and A. Beygelzimer and F. d'Alché-Buc and E. Fox and R. Garnett (Curran Associates, Inc.), 8024–8035. https://papers.nips.cc/paper/9015-pytorch-an-imperative-style-high-performance-deep-learning-library

Punturo, M., Abernathy, M., Acernese, F., et al. 2010, Classical and Quantum Gravity, 27, 084007, doi: 10.1088/0264-9381/27/8/084007

Reitze, D., et al. 2019, Bull. Am. Astron. Soc., 51, 035. https://arxiv.org/abs/1907.04833

Sachdev, S., et al. 2019. https://arxiv.org/abs/1901.08580

Schmidt, P., Ohme, F., & Hannam, M. 2015, Phys. Rev., D91, 024043, doi: 10.1103/PhysRevD.91.024043

Schneider, P., Ehlers, J., & Falco, E. E. 1992, Gravitational Lenses (New York: Springer), 112, doi: 10.1007/978-3-662-03758-4

Sereno, M., Jetzer, P., Sesana, A., & Volonteri, M. 2011, MNRAS, 415, 2773, doi: 10.1111/j.1365-2966.2011.18895.x

Shoemaker, D. 2009, Advanced LIGO anticipated sensitivity curves, Tech. Rep. LIGO-T0900288, LIGO Scientific Collaboration

Simonyan, K., & Zisserman, A. 2014, ArXiv e-prints. https://arxiv.org/abs/1409.1556

Singh, A., Li, I., Hannuksela, O., Li, T., & Kim, K. 2019, American Journal of Undergraduate Research, 16, 5–16, doi: 10.33697/ajur.2019.019

Springenberg, J. T., Dosovitskiy, A., Brox, T., & Riedmiller, M. 2014, arXiv e-prints, arXiv:1412.6806. https://arxiv.org/abs/1412.6806

Szegedy, C., Ioffe, S., & Vanhoucke, V. 2016, CoRR. https://arxiv.org/abs/1602.07261

Szegedy, C., Vanhoucke, V., Ioffe, S., Shlens, J., & Wojna, Z. 2015, CoRR. https://arxiv.org/abs/1512.00567

Szegedy, C., Liu, W., Jia, Y., et al. 2014, CoRR. https://arxiv.org/abs/1409.4842

Takahashi, R., & Nakamura, T. 2003, Astrophys. J., 595, 1039. http://stacks.iop.org/0004-637X/595/i=2/a=1039

Thorne, K. S. 1983, in Gravitational Radiation, ed. N. Deruelle & T. Piran, Amsterdam: North Holland

Usman, S. A., et al. 2016, Class. Quant. Grav., 33, 215004, doi: 10.1088/0264-9381/33/21/215004